

# High-strength and high-conductivity Cu-0.7Mg-0.1Ca alloy fabricated via heat treatment and severe plastic deformation

A. Kalhor <sup>a,\*</sup>, K. Rodak <sup>a</sup>, H. Myalska-Głowacka <sup>a</sup>, B. Chmiela <sup>a</sup>, K. Kuglarz <sup>b</sup>, I. Schindler <sup>c</sup>, K. Radwański <sup>d</sup>, M. Kampik <sup>e</sup>

<sup>a</sup> Faculty of Materials Engineering, Silesian University of Technology, Krasińskiego 8, 40-019, Katowice, Poland

<sup>b</sup> Faculty of Materials Engineering and Industrial Computer Science, AGH University of Science and Technology, 30 Mickiewicza, 30-059, Kraków, Poland

<sup>c</sup> VŠB – Technical University of Ostrava, Faculty of Materials Science and Technology, 17. listopadu 2172/15, 70800 Ostrava, Czech Republic

<sup>d</sup> Materials Research Group, Łukasiewicz Upper Silesian Institute of Technology, Karola Miarki 12-14, 44-100, Gliwice, Poland

<sup>e</sup> Faculty of Electrical Engineering, Silesian University of Technology, 44-100, Gliwice, Poland

(Received 17 October 2024; Accepted 09 April 2025)

## Abstract

In this research, the impact of annealing combined with severe plastic deformation (SPD) applied through the MaxStrain component of the Gleeble thermo-mechanical testing device on the microstructural characteristics, tensile behavior, and electrical conductivity of a Cu-0.7Mg-0.1Ca (wt%) alloy was examined. The as-cast material underwent two treatments: annealing at 923 K for 15 min followed by cooling in the air, and annealing at 923 K for 75 min followed by quenching in agitated water, which resulted in irregular and partially spheroidized Cu<sub>5</sub>Ca particles, respectively. The subsequent MaxStrain deformation resulted in a remarkable grain refinement through dynamic recrystallization (DRX), for which a greater DRX percentage was obtained for the annealed and quenched specimen compared to the annealed and air-cooled one. As a consequence, the annealed and quenched specimen showed a better strength-ductility synergy, while these improvements came with only a ~1% reduction in the electrical conductivity. Accordingly, the present work revealed that annealing and subsequent SPD processing serves as an effective method for processing high-strength and high-conductivity (HSHC) copper alloys.

**Keywords:** Annealing; MaxStrain deformation; Simulation; Microstructure; Tensile properties; Four-wire Kelvin resistance measurement

## 1. Introduction

For more than a century, copper and its derivative alloys have found widespread applications across multiple sectors because of their outstanding electrical and thermal properties [1–4]. Meanwhile, the rise of new technologies like electric automobiles and next-generation mobile networks infrastructure is driving up the need for high-strength and high-conductivity (HSHC) copper alloys, which can provide an appropriate combination of enhanced mechanical properties along with satisfactory electrical conductivity [5–8]. Generally, HSHC copper alloys exhibit tensile strengths that are 1.5 to 4 times greater than those of pure copper (ranging from 300 to 800 MPa) and electrical conductivities between 50% and 95% of the value for pure copper [9]. Pure copper in annealed condition possesses the values of 58 MS/m as its electrical conductivity, which is recognized as the 100% standard for international annealed copper (IACS) [10,11]. HSHC copper alloys normally attain their good mechanical properties via a combination of different strengthening methods, including solid-solution strengthening [12,13], precipitation hardening [14,15], deformation strengthening [16,17], grain refinement [18,19], and composite strengthening [20]. However, the formation of crystal defects (imperfections in the atomic arrangement of a material such as vacancies, solute atoms in the lattice, dislocations, grain boundaries, and second-phase particles) through the mentioned approaches leads to higher electron scattering and, consequently, has an adverse impact on the electrical conductivity of the alloy [21–23]. Consequently, attaining both exceptional strength and

\* Corresponding author | Email: [alireza.kalhor@polsl.pl](mailto:alireza.kalhor@polsl.pl) | ORCID: 0000-0001-7426-0735

superior electrical conductivity at the same time presents a significant difficulty in improving the functionality of HSHC copper alloys [24–26].

As of now, Cu-Mg alloys, which are well known for their remarkable mechanical properties and good electrical conductivity, represent one of the major categories of HCHC copper alloys [27]. Thanks to their capability to offer satisfactory electrical conductivity while withstanding high loads, Cu-Mg alloys have so far been effectively employed in a broad spectrum of industrial applications, such as express rail contact cables [28–32]. Cu-Mg alloys also benefit from the lightweight nature of magnesium compared to heavier alloys like Cu-Ni and Cu-Cr alloys, which makes them a more appealing option for weight-sensitive applications. In the meantime, it has also been observed that Cu-Mg alloys can experience further enhancement in mechanical properties through the addition of other alloying elements [33–35] as well as deformation strengthening [36–39]. However, when it comes to alloying, attention should be dedicated to the careful selection of those elements that have a less deteriorative effect in terms of electrical conductivity. In this regard, it has been reported that the incorporation of calcium into copper has a less negative impact on the electrical conductivity relative to the addition of other elements, including nickel, tin, manganese, aluminum, cobalt, iron, and silicon [28,40].

It has also been observed that calcium addition, along with deformation strengthening, results in a ternary Cu-Mg-Ca alloy with remarkable mechanical properties while having satisfactory electrical conductivity [28,35]. Moreover, in a similar processing condition, ternary Cu-Mg-Ca alloys can exhibit better mechanical properties relative to their binary Cu-Mg counterparts. For instance, the study of Ma et al. [30] can be mentioned, wherein they utilized equal-channel angular pressing (ECAP) on Cu-0.43Mg (wt%) and Cu-0.41Mg-0.06Ca (wt%) alloys through route B<sub>C</sub> at ambient temperature and noticed that their developed ternary alloy consistently exhibited greater hardness and yield strength than the binary alloy throughout all passes of ECAP processing. In another study, Kalhor et al. [35] applied severe plastic deformation through the MaxStrain component of the Gleeble thermo-mechanical testing device to Cu-0.7Mg (wt%) and Cu-0.7Mg-0.1Ca (wt%) alloys and determined that the MaxStrain-deformed ternary alloy had greater yield strength and tensile strength than the binary alloy.

In the present investigation, concentrations of 0.7 wt% magnesium and 0.1 wt% calcium were chosen and added to pure copper to develop a ternary Cu-Mg-Ca alloy. These concentrations were intentionally selected to incorporate two different strengthening mechanisms into the alloy. Regarding magnesium, a concentration of 0.7 wt% falls beneath the minimum level required for the Cu<sub>2</sub>Mg intermetallic phase to form in Cu-Mg alloys [41], and only leads to the solid-solution strengthening in the alloy. In contrast, calcium has a very low solubility in copper, and the addition of even a small quantity of calcium leads to the formation of the Cu<sub>5</sub>Ca intermetallic phase within the material [42]. Hence, the addition of even a small amount of 0.1 wt% calcium provides second-phase hardening for the alloy without a considerable loss in its electrical conductivity. Furthermore, this specific chemical composition and element ratio have not been studied before, which could provide valuable insights for future research. The as-cast specimens were then annealed for variable durations of time and cooling rates before being exposed to severe plastic deformation (SPD) through MaxStrain deformation, and their microstructural features, hardness and tensile properties, as well as electrical conductivity, were assessed at various stages, and the obtained outcomes are presented and explained in the following sections.

## 2. Materials and Methods

### 2.1. Alloy Development

The alloy was fabricated by melting high-purity (99.99 wt%) rods of the constituent elements in a boron nitride-coated graphite crucible inside induction furnace maintained under a consistent argon gas flow. The melt was then poured into a preheated steel mold 43 mm in diameter and 200 mm in length and allowed to air cool to ambient temperature. Subsequently, the casting surface imperfections were eliminated from the as-cast billet through machining, and dictated by the requirements of the MaxStrain process, specimens measuring 10 × 10 × 27.2 mm<sup>3</sup> were precisely extracted from the lengthwise orientation of the billets. The concentrations of elements in the alloy were evaluated using energy dispersive X-ray spectroscopy (EDS) at 10 different spots on the freshly polished surface of the material, and the obtained results are presented in Table 1. To ensure that the EDS results are accurate and reliable, the analyses were conducted using the well-known PROZA correction technique and certified reference materials containing ultra-pure copper

and magnesium (both 99.999 wt%) from reliably proven Astimex Standards (METM25-44), as well as calcium from calcium sulfate (MINM25-53).

**Table 1:** Elemental composition of the as-cast material.

Element	Copper	Magnesium	Calcium	Impurity atoms
Concentration (wt%)	99.17 ± 0.05	0.71 ± 0.06	0.12 ± 0.04	< 0.01

The as-cast material was next exposed to thermal treatment procedures, consisting of either annealing at 923 K for 15 min with subsequent cooling in the air to ambient temperature or annealing at 923 K for 75 min followed by quenching in water to ambient temperature. Specifically, the latter heat treatment process aimed to accomplish three main purposes. Firstly, it aimed to homogenize the arrangement of magnesium atoms within the single-phase Cu-Mg matrix. Secondly, the sufficiently long annealing duration was intended to enhance the plasticity of the alloy via reducing the irregularity of the morphologies of Cu<sub>5</sub>Ca particles within the as-cast material. Thirdly, the quenching aimed to establish residual thermal stress in the alloy as a consequence of the distinct coefficients of thermal expansion (CTE) between the Cu-Mg solid-solution matrix and the Cu<sub>5</sub>Ca intermetallic particles.

## 2.2. MaxStrain Processing

In general, the MaxStrain process involves controlled deformation of the central segment of a square prism specimen by pressing it with two anvils in 180° opposite directions. Following the first compression, the specimen rotates 90° around its lengthwise axis and is compressed again in the direction perpendicular to its previous compression direction, and this cycle continues until the desired amount of accumulated strain is obtained within the specimen [35,43]. Applied force, anvil velocity, strike, and temperature are among the primary process variables in MaxStrain processing, which can be precisely controlled throughout the whole deformation process [44]. A simplified graphical representation of the MaxStrain component within the Gleeble thermo-mechanical testing device is illustrated in Figure 1. The MaxStrain specimen can be constrained or unconstrained (free-end) at either side of the specimen during deformation [45]. In constrained deformation, the material demonstrates plastic flow in transverse directions, while in the free-end mode, it primarily flows along the length. Consequently, the constrained specimen retains a length close to its original state post-deformation, whereas the longitudinal dimension of the free-end specimen expands as a result of the deformation process.

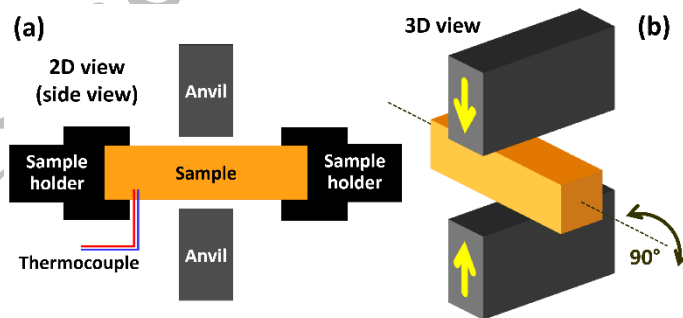


**Figure 1:** Simplified graphical representation of the MaxStrain component of the Gleeble thermo-mechanical testing device shown in (a) 2D (side view) and (b) 3D views.

In this study, the MaxStrain operation was performed in the free-end mode with molybdenum disulfide (MoS<sub>2</sub>) lubricant being applied on either end of the specimen holders in order to minimize friction and facilitate specimen expansion in the lengthwise direction. The whole deformation process was carried out at ambient temperature for 20 passes, using the strike pattern shown in Figure 2. In order to monitor temperature changes during the full course of deformation, a thermocouple was installed at the lateral edge of the specimens. Yet, the recorded mean temperature was about 305.65 K (32.5 °C), with a measured peak temperature of approximately 310 K (37 °C), making the temperature rise negligible in this experiment. In fact, the remarkable heat conductivity of the alloy allowed for the rapid transfer of thermal energy to the

tool-steel specimen holders and the surrounding equipment, effectively minimizing heat buildup and preventing temperature rise during deformation. Table 2 provides an overview of the fabrication history for each specimen, along with the abbreviated names that are assigned to refer to them henceforth.

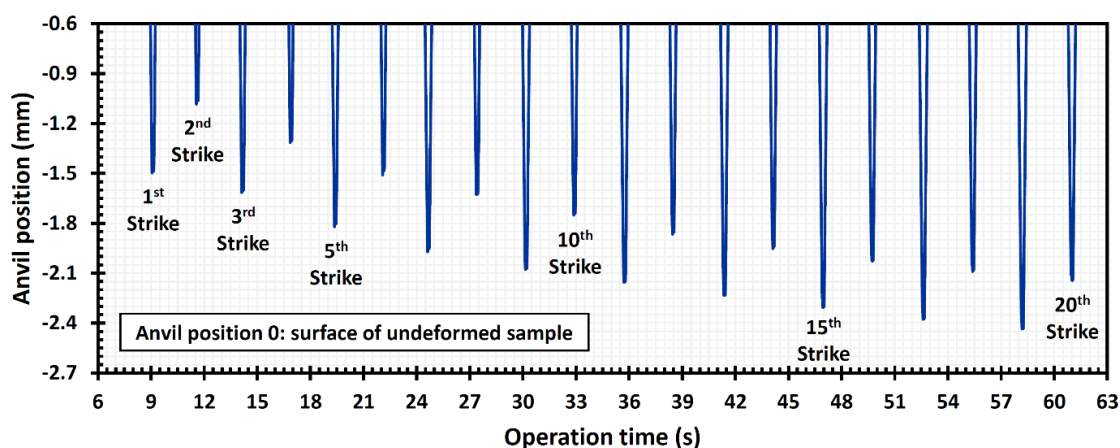


**Figure 2:** Schematic of strike pattern for MaxStrain deformation in this study.

**Table 2:** The summary of processing steps and abbreviated names of the specimens.

Processing history	Name
As-cast material → Annealing at 923 K for 15 min → Cooling in the air to ambient temperature	A15
As-cast material → Annealing at 923 K for 75 min → Quenching to ambient temperature	A75
A15 specimen → MaxStrain processing for 20 passes at ambient temperature	M15
M15 specimen → MaxStrain processing for 20 passes at ambient temperature	M75

### 2.3. Microstructural Characterization

Backscatter electron (BSE) imaging and element mapping were conducted using a Tescan Mira scanning electron microscope (SEM), utilizing primary electron beam energy of 15 keV. Fractographic examination was conducted on a Hitachi S-3400N SEM, also set to a 15 keV primary electron beam. Additionally, electron backscatter diffraction (EBSD) mapping was carried out on an Inspect JEOM SEM equipped with an EDAX detector, operating at an acceleration voltage set to 20 kV.

### 2.4. Mechanical Properties Measurements

Hardness and tensile strength evaluations were carried out to assess the mechanical properties of the samples. For hardness measurement, the Vickers technique was utilized, applying a 1 kg load (HV1) and maintaining a dwell duration of 10 s on a Struers Duramin A300 hardness testing machine. Due to the small dimensions of the plastic deformation region in MaxStrain-deformed specimens, tensile tests had to be conducted on mini-specimens, with dimensions illustrated in Figure 3. These mini-specimens were carefully cut from the central portion of the plastic deformation region, aligned in the transverse direction, and oriented perpendicular to the 20th pass pressing direction. The tensile testing was carried out utilizing an MST QTest/10 device at ambient temperature with the starting strain rate set to  $1 \times 10^{-3} \text{ s}^{-1}$  and three measurements for each specimen.

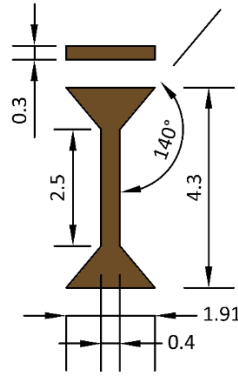


**Figure 3:** Geometrical parameters of tensile test mini-specimens (units are in mm).

## 2.5. Determination of Electrical Conductivity

Electrical conductivity measurements were performed using the widely recognized four-wire Kelvin resistance method, which is highly effective for measuring electrical conductivity in small samples. To facilitate this, specimens with a surface area of approximately 2 mm<sup>2</sup> and a length measuring 4 mm were extracted from the same orientation as the tensile mini-specimens. Then, an electrical current of 750 mA was applied to the terminal points of the specimens, and the voltage difference was measured. The current source was a Fluke 5700A calibrator, and the voltage was measured using a Keithley 2182A nanovoltmeter. A simplified schematic representation of the four-wire Kelvin resistance measurement arrangement is depicted in Figure 4.

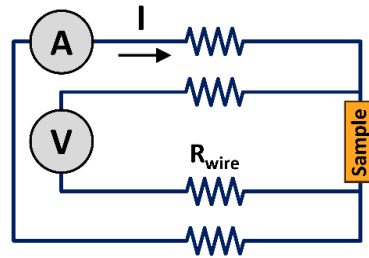


**Figure 4:** Simplified schematic representation of the four-wire Kelvin resistance testing device.

## 3. Results and Discussion

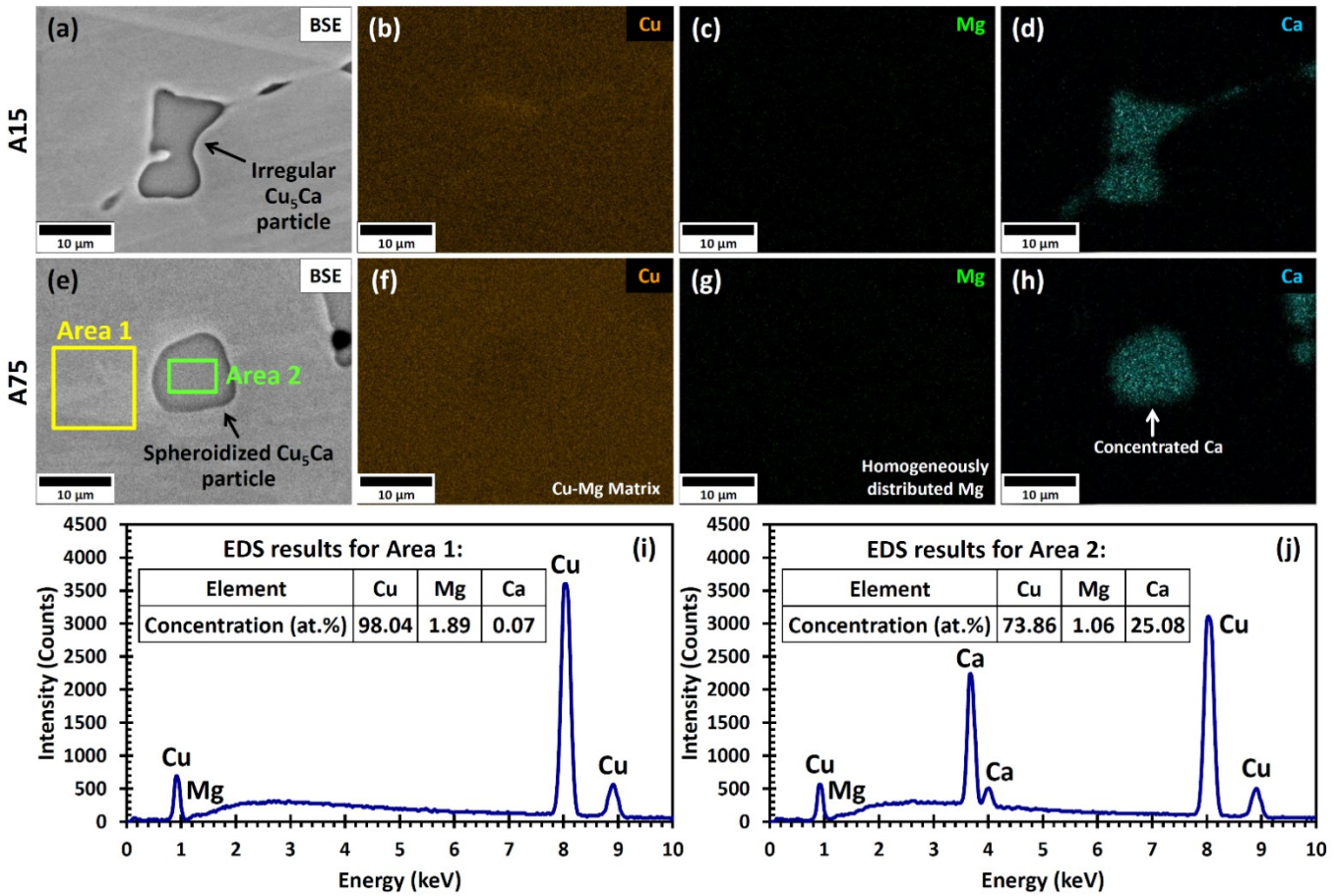
### 3.1. Characterization of the Initial Specimens

Figure 5 shows the microstructures of the initial specimens, the element mapping analysis results for them, and the EDS compositional breakdown regarding the matrix and the second-phase particles in the A75 specimen. The observation indicates that in both specimens, the second-phase particles, averaging  $8.3 \pm 3.7 \mu\text{m}$  in size, are uniformly dispersed throughout the matrix. Considering the chemical formulation of the developed alloy and the binary phase diagrams associated with the Cu-Mg and Cu-Ca systems [35], these second-phase particles were expected to be Cu<sub>5</sub>Ca intermetallic compound. In order to confirm this assumption, both specimens underwent element mapping analysis, and the A75 specimen also received EDS analysis for a more precise identification of the matrix as well as second-phase particles. Figures 5(b), 5(c), and 5(d) respectively show the distribution of copper, magnesium, and calcium elements in Figure 5(a), and Figures 5(f), 5(g), and 5(h) respectively illustrate the dispersion of these elements in Figure 5(e), demonstrating that in both the A15 and A75 specimens, magnesium atoms are homogeneously distributed throughout the matrix in a solid-solution state, whereas calcium atoms are aggregated into the second-phase particles.

Figure 5(i) shows the EDS results corresponding to area 1 marked in Figure 5(e), confirming that the matrix phase comprises a solid-solution where magnesium is integrated into copper, thereby approving the initial assumption. Alternatively, Figure 5(j) presents the EDS results corresponding to area 2, revealing that the second-phase particles are composed of copper and calcium with a copper-to-calcium at% ratio of  $\sim 3$ , which is indicative of the Cu<sub>5</sub>Ca intermetallic compound, with an ideal copper-to-calcium at% ratio of



5. Li et al. [28] also observed the presence of  $\text{Cu}_5\text{Ca}$  intermetallic particles in  $\text{Cu-0.29Mg-0.21Ca}$  (wt.%) alloy. A comparison between Figures 5(a) and 5(b) also demonstrates the partial spheroidization observed in the  $\text{Cu}_5\text{Ca}$  particles in the A75 specimen, which demonstrates the significance of the 75-min annealing. It must be noted that this partial spheroidization did not completely affect all  $\text{Cu}_5\text{Ca}$  particles dispersed within the microstructure of the A75 specimen; however, it reduced their irregularity.



**Figure 5:** (a) SEM-BSE image, and element mapping analysis results for (b) copper, (c) magnesium, and (d) calcium elements in A15 specimen; (e) SEM-BSE image, and element mapping analysis results for (f) copper, (g) magnesium, and (h) calcium elements in A75 specimen; EDS results for (i) area 1, and (j) area 2 marked in (e).

### 3.2. Mapping of Equivalent Strain Distribution

The barreling effect, which occurred during MaxStrain deformation, caused significant geometric distortion, making it unfeasible to determine equivalent strain using conventional mathematical formulas. As a consequence, the entire MaxStrain deformation process was modeled using finite element analysis with FORGE® NxT software to accurately determine the equivalent strain across the specimen. Similar to the actual deformation conditions, in the simulation, the anvils were positioned 8 mm higher than the top surface of the uncompressed specimen before the start of each pressing step. Next, the ultimate anvil heights for each pass, which were derived using experimental data (see Figure 2), were fed into the software to establish the anvil movement per strike. Figures 6(a) to 6(c) display the simulation outcomes for the primary halves of the specimen, with cross-sectional planes along the major directions applied at the center to visualize the internal equivalent strain distribution throughout the specimen. According to the simulation results, it was determined that the maximum equivalent strain occurred at the center of the central transverse plane, reaching a value of 3.5, and gradually decreased by moving outward from the center toward the edges and corners of this plane. Likewise, in both major longitudinal planes shown in Figures 6(b) and 6(c), the value of equivalent strain was calculated to be the highest at the central point of the plastic deformation region (equivalent to 3.5) and decreased by moving from the center toward major directions. According to the simulation results, the highest strain-hardening effect was anticipated to occur at the central location of

the plastic deformation region, where the highest equivalent strain was achieved. Hence, the microstructural analyses were intentionally conducted in this region.

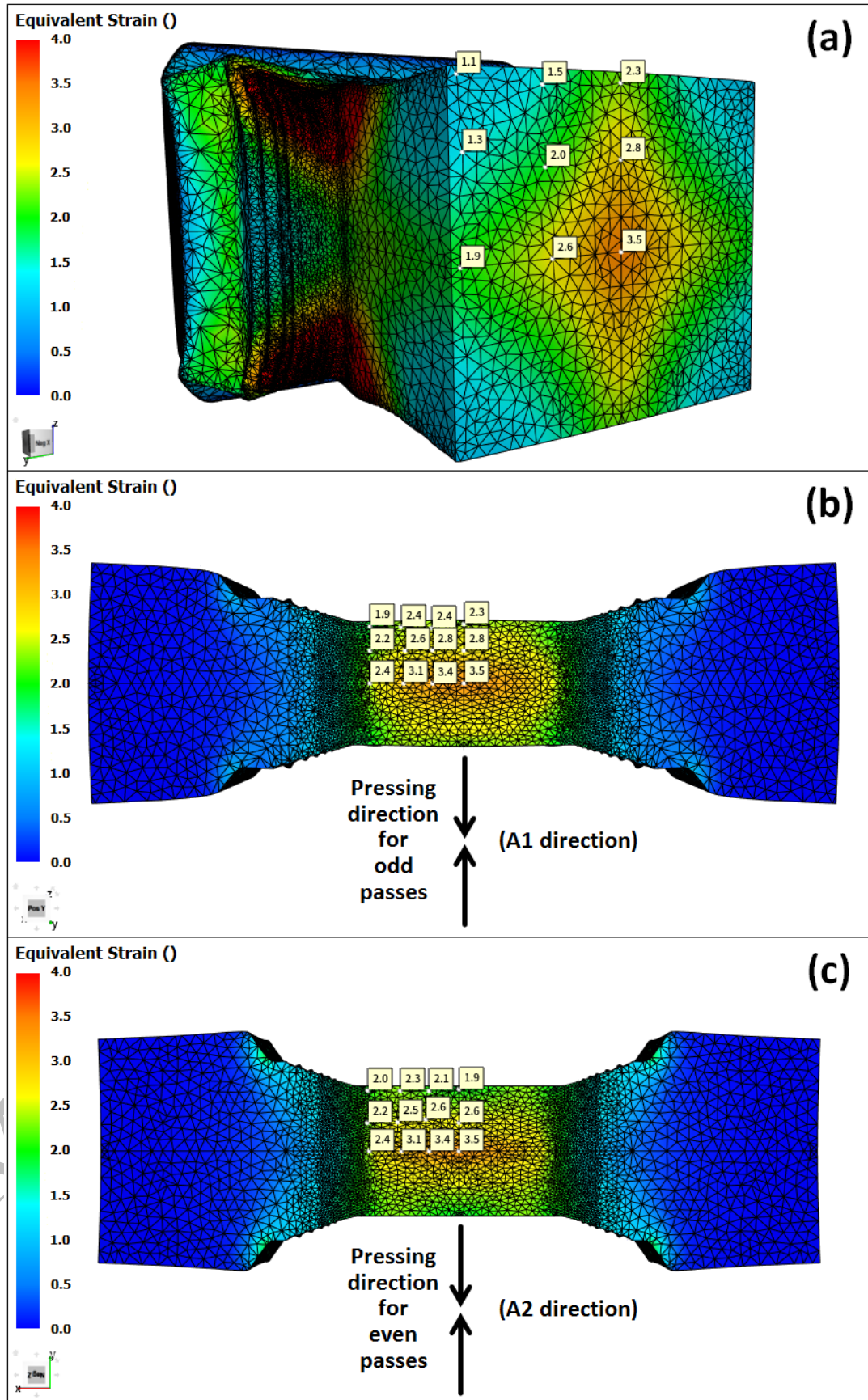


**Figure 6:** Simulation results showing the pattern of equivalent strain in (a) central transverse, (b) central longitudinal (X-Z), and (c) central longitudinal (X-Y) planes.



### 3.3. Microstructural Features following MaxStrain Deformation

The inverse pole figure (IPF) maps obtained from the EBSD data for the center of the central transverse plane within the plastic deformation region of the M15 and M75 specimens are respectively shown in Figures 7(a) and 7(c). The lengths of these IPF maps are oriented perpendicular to the A2 direction (the pressing direction for even passes), and high-angle grain boundaries (HAGBs) with  $15^\circ \leq \theta$  are highlighted by black lines in them. Given the challenges associated with identifying second-phase particles through the EBSD technique, the IPF maps were specifically obtained from the Cu-Mg matrix phase, and SEM analysis was utilized to investigate the  $\text{Cu}_5\text{Ca}$  intermetallic particles. The EBSD analysis results demonstrated that the M15 specimen had a mean grain size of  $4.5 \pm 1.1 \mu\text{m}$ , and the M75 specimen possessed a mean grain size of  $2.4 \pm 0.6 \mu\text{m}$ .

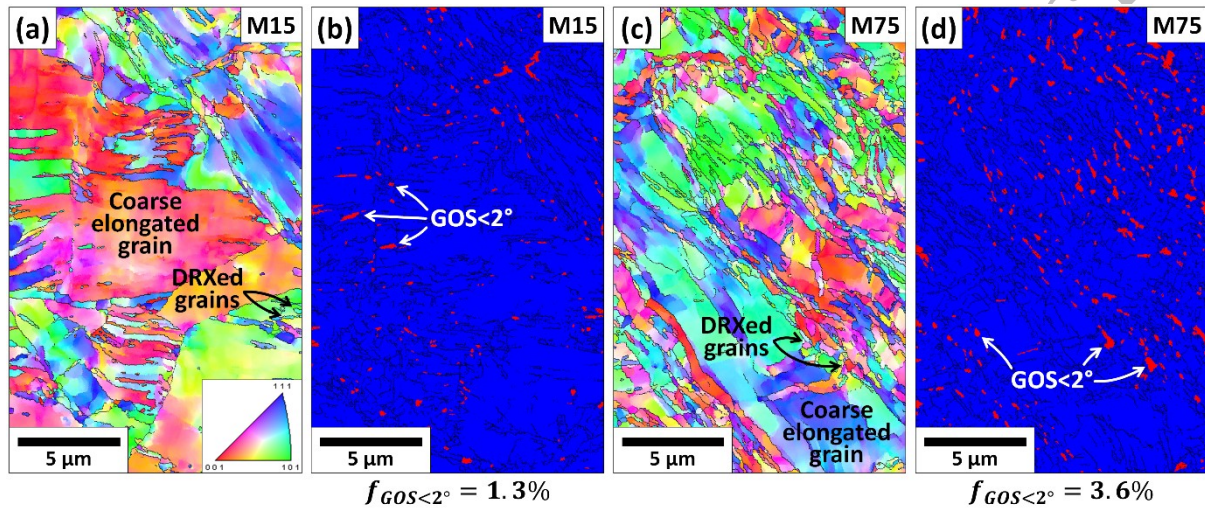


**Figure 7:** (a) IPF map, and (b) GOS map of the M15 specimen; (c) IPF map, and (d) GOS map of the M75 specimen.

The EBSD results reveal that the 75-min annealing at 923 K followed by quenching in agitated water conducted before MaxStrain processing has led to a greater degree of grain refinement in the MaxStrain-deformed specimen. This observation can be explained by considering the critical role of the  $\text{Cu}_5\text{Ca}$  intermetallic particles. It is well-established that copper has a face-centered cubic (FCC) crystal structure with lattice constants of  $a = b = c = 3.615 \text{ \AA}$  and  $\alpha = \beta = \gamma = 90^\circ$  [46,47], as illustrated in Figure 8(a). Given the low magnesium content within the elemental composition of the developed alloy (0.7 wt%), the dissolving magnesium atoms in the copper matrix form a substitutional solid-solution by replacing some copper atoms in the FCC lattice. Therefore, the dominant crystal structure of the matrix in the alloy remains FCC, and the minor amount of magnesium dissolved in copper exerts no significant effect on the crystal structure of the matrix. On the other hand, the  $\text{Cu}_5\text{Ca}$  unit cell shown in Figure 8(b) has lattice constants of  $a = b = 5.074 \text{ \AA}$  and  $c = 4.074 \text{ \AA}$ , and  $\alpha = \beta = 90^\circ$  and  $\gamma = 120^\circ$ , which aligns with the hexagonal crystal system [48]. Due to the mismatch in the crystal structures of the single-phase Cu-Mg solid-solution matrix and the  $\text{Cu}_5\text{Ca}$  intermetallic particles, their properties, including CTE, are also different. In the instance of the A75 specimen, upon heating to 923 K, both the Cu-Mg matrix and  $\text{Cu}_5\text{Ca}$  particles underwent volume expansion. Due to the varying CTE values of the Cu-Mg matrix and  $\text{Cu}_5\text{Ca}$  particles, the density of dislocations in the Cu-Mg matrix near the  $\text{Cu}_5\text{Ca}$  particles rose at the initiation of the annealing process. However, by the conclusion of the 75-min soaking period, it reverted to a new stable equilibrium state. Subsequently, a non-equilibrium temperature change occurred when the alloy was quenched to ambient temperature, during which both the Cu-Mg matrix and the  $\text{Cu}_5\text{Ca}$  particles encountered rapid thermal shrinkage, leading to the formation of a new set of dislocations around the  $\text{Cu}_5\text{Ca}$  particles in the Cu-Mg matrix to maintain the structural cohesion of the alloy. The increased dislocation density observed in the A75 specimen, in contrast to the A15 specimen, facilitated the development of dislocation cell structures during the MaxStrain operation. These cell structures subsequently evolved into low-angle grain boundaries



(LAGBs) with  $2^\circ \leq \theta < 15^\circ$  and eventually into HAGBs over the course of 20 passes of the MaxStrain deformation. This interpretation accounts for the more intensified grain refinement observed in the M75 specimen compared to the M15 specimen.

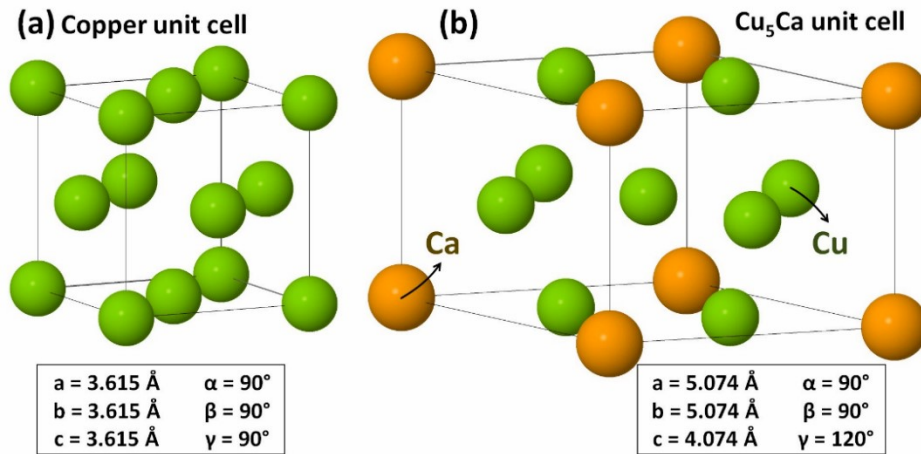


**Figure 8:** Schematic illustrations of the crystal structures of (a) copper [47], and (b)  $\text{Cu}_5\text{Ca}$  [48] unit cells.

The greater degree of grain refinement in the M75 specimen compared to the M15 specimen becomes more apparent when comparing the grain orientation spread (GOS) maps derived from EBSD data. In general, GOS reflects the mean difference in orientation between the mean orientation of a grain and all individual measurements within that grain, and it enables the differentiation of recrystallized grains (characterized by a GOS below a certain threshold) from deformed grains (having a GOS quantity exceeding that threshold) and the assessment of the proportion of recrystallized grains [35]. Consistent with prior research [49–51], the critical GOS quantity of  $2^\circ$  was considered to differentiate between recrystallized grains and those deformed grains in this study. Figures 7(b) and 7(d), respectively, display the GOS maps of the M15 and M75 specimens at the same location as Figures 7(a) and 7(c). In the presented GOS maps, grains with GOS quantities under  $2^\circ$  are displayed in red, grains with GOS quantities of  $2^\circ$  or higher are outlined in blue, and LAGBs are highlighted with black outlines. Thus, the red spots in these GOS maps can be considered recrystallized grains, while the blue areas represent deformed grains. The higher percentage of grains exhibiting a GOS quantity less than  $2^\circ$  in the M75 specimen compared to the M15 specimen demonstrates the greater effectiveness of the 75-min annealing and quenching heat treatment route over the 15-min annealing and cooling in the air route in promoting dynamic recrystallization (DRX, formation of new strain-free grains during high-temperature deformation) during MaxStrain deformation. However, it must be noted that relying merely on GOS data to evaluate grain refinement is insufficient in this investigation since, due to 20 cycles of repetitive deformation, early-stage recrystallized grains have undergone subsequent deformation, finally resulting in GOS quantities greater than  $2^\circ$ . Nonetheless, the proportion of grains possessing a GOS quantity lower than  $2^\circ$  is an appropriate metric for comparing the comparative degree of the occurrence of recrystallization between specimens.

The next remarkable observation from the IPF maps is the heterogeneous grain structure, characterized by the presence of both coarse elongated grains as well as fine equiaxed ones. This grain morphology indicates the occurrence of partial DRX as a consequence of conducting the MaxStrain operation at ambient temperature, which is below the typical temperature required for full DRX in copper alloys [52,53]. Figure 9 presents the range of misorientation angles measured in the specimens subjected to MaxStrain deformation. Comparing these distributions reveals a higher percentage of HAGBs in the M75 specimen compared to the M15 specimen, which aligns with the earlier discussion, demonstrating that the 75-min annealing and subsequent quenching in agitated water has facilitated more substantial grain refinement after MaxStrain processing compared to the 15-min annealing and subsequent cooling in the air. It was also observed that the  $\text{Cu}_5\text{Ca}$  particles remained undeformed even after 20 passes of MaxStrain deformation. However, some of these particles exhibited cracks following the deformation, as shown by the arrows in Figures 10(a) and 10(b) for the  $\text{Cu}_5\text{Ca}$  particles in the M15 and M75 specimens, respectively.

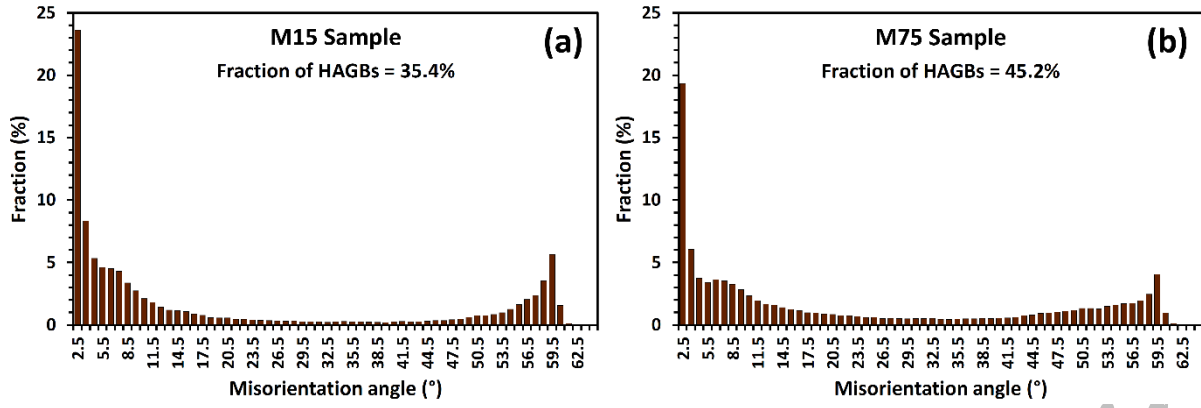


**Figure 9:** Distribution pattern of misorientation angles (a) M15, and (b) M75 specimens.

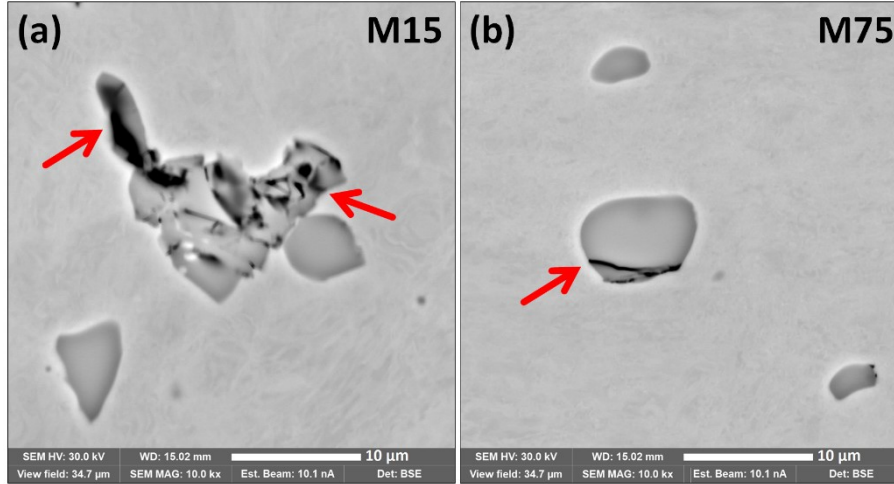


**Figure 10:** SEM-BSE images of  $\text{Cu}_5\text{Ca}$  intermetallic particles in (a) M15, and (b) M75 specimens.

### 3.4. Mechanical Properties

The A15 and A75 specimens possessed mean hardness values of  $78 \pm 4$  HV and  $81 \pm 4$  HV, respectively. These values show that the 75-min annealing and subsequent quenching in agitated water led to a 4% increase in mean hardness compared to the 15-min annealing and subsequent cooling in the air, which arises from the larger density of dislocations in the A75 specimen, as previously discussed. Regarding the M15 and M75 specimens, obtaining a consistent mean hardness value was infeasible due to the internal strain heterogeneity, as shown in Figure 6. Therefore, for the M15 and M75 specimens, the hardness indentations were performed along the A1 and A2 directions at regular 0.45 mm intervals in the central transverse plane. Figures 11(a) and 11(b) show the obtained values for these hardness measurements and clearly demonstrate a correlation between hardness and equivalent strain in M15 and M75 specimens. Notably, the hardness profile aligns with the pattern of equivalent strain, showing that the central part of the plastic deformation region displays greater hardness than both the middle and edge areas. This suggests a more pronounced strain hardening effect in the center, attributed to the increased equivalent strain concentrated in that region. However, some indentations deviated from this general trend, which can be ascribed to the existence of  $\text{Cu}_5\text{Ca}$  intermetallic particles. These particles, when positioned near or directly beneath the indentation point, influenced the local hardness. The inherent hardness of  $\text{Cu}_5\text{Ca}$  intermetallics (which is notably higher than the value for the surrounding copper matrix) caused localized hardening effects. As a result, the indenter encountered more resistance, leading to higher measured hardness values in these specific regions, which resulted in these deviations from the overall trend.

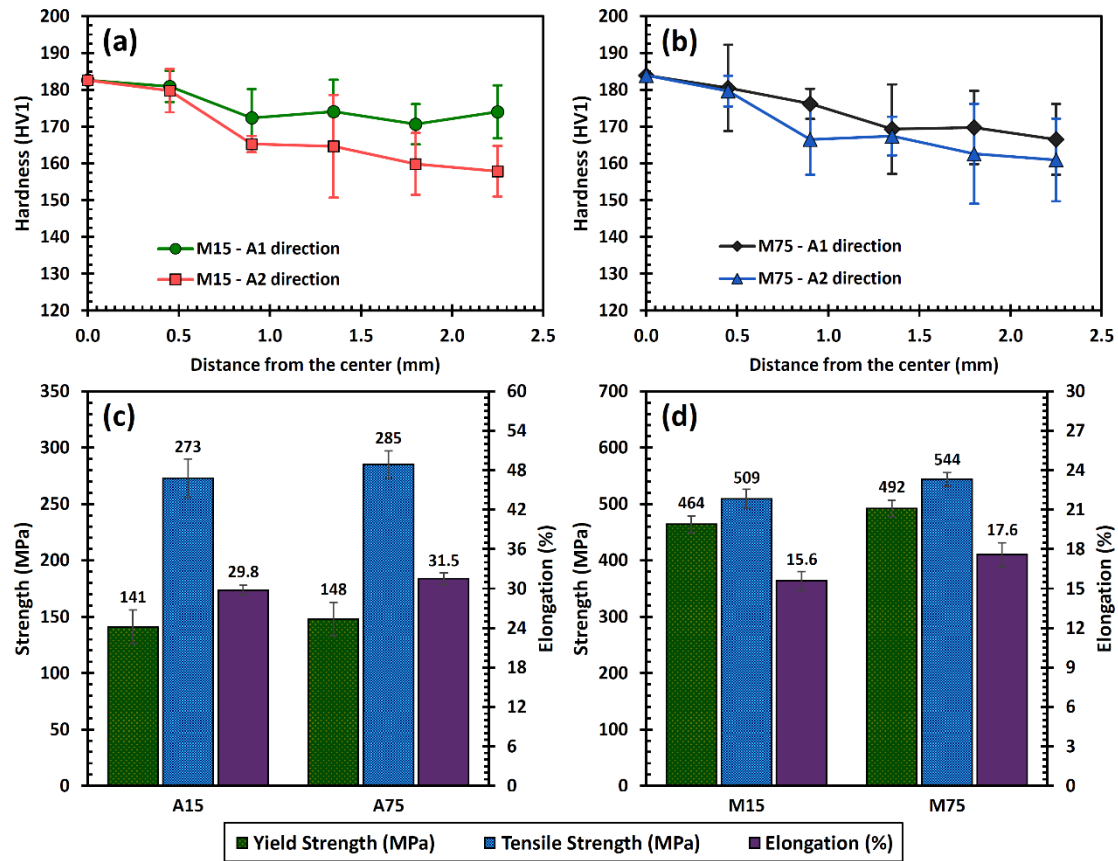


**Figure 11:** Hardness test results for (a) M15, and (b) M75 specimens; tensile test results for (c) initial, and (d) MaxStrain-deformed specimens.

Figures 11(c) and 11(d), respectively, present the tensile properties measurements for the initial and MaxStrain-deformed specimens. Given the small size of the mini-specimens employed for the tensile test, it was not feasible to use an extensometer for measuring displacement in this study. Hence, to ensure reliable results, the elongation values were calculated using the measured lengths of the individual broken fragments shown in Figures 12(a) and 12(b). The results of the tensile testing for the initial specimens showed that the A75 specimen had 5% higher yield strength, 4% higher tensile strength, and 6% greater elongation in comparison with the A15 specimen. The improvements in strength may be ascribed to the increased density of dislocations along with the existence of residual thermal stresses in the A75 specimen relative to the A15 specimen, and the improvement in ductility can be ascribed to the more microstructural homogeneity as well as less irregularity of the  $\text{Cu}_5\text{Ca}$  particles in the A75 specimen. More specifically, the irregular  $\text{Cu}_5\text{Ca}$  particles in the A15 specimen acted as focal points for stress concentration during deformation and promoted crack formation, whereas partially spheroidized  $\text{Cu}_5\text{Ca}$  particles in the A75 specimen provided a more uniform stress distribution nearby these particles during the tensile test and led to a slight enhancement in its elongation.

In the meantime, it is evident that the MaxStrain processing significantly improved the tensile strengths of both specimens. Relative to their initial counterparts, M15 and M75 specimens exhibited respective increases of 229% and 232% in yield strength and 86% and 91% in tensile strength. Yet, these improvements came at the cost of decreasing elongation by 48% and 44% for the M15 and M75 specimens, respectively. Again, the explanation for these enhancements in yield strength and tensile strength lies in the processing history of the specimens. To clarify further, during the MaxStrain operation, repetitive deformation generated a high density of dislocations within the severely deformed grains, especially in the vicinity of the  $\text{Cu}_5\text{Ca}$  intermetallic particles. Moreover, it also facilitated grain refinement by transforming the large original grains into smaller ones via DRX, which in turn elevated the percentage of HAGBs. This simultaneous increase in dislocation density and grain boundary density effectively impeded dislocation



mobility and caused a greater resistance to slip and an improved hindrance to sliding, and eventually resulted in the enhancement of the mechanical properties of the specimens.

The broken fragments and the fracture surface of the M15 specimen are respectively shown in Figures 12(a) and 12(c). This specimen demonstrated a moderate level of elongation to failure of 15.6%, which is in the usual range of the typical elongation value recorded for SPD processed Cu-Mg alloys [30,37,54]. Likewise, Figures 12(b) and 12(d) respectively present the broken pieces together with the fracture surface of the M75 specimen, which exhibited a slightly better elongation value of 17.6%, attributable to the relatively better homogenization of the initial as-cast microstructure accomplished through a longer annealing process compared to the M15 specimen. The occurrence of a heterogeneous dimple structure on the fracture surfaces of both specimens is consistent with their heterogeneous microstructure, with large dimples corresponding to the coarse and elongated grains and small dimples representing the fine recrystallized grains. Nearly undeformed but fragmented  $\text{Cu}_5\text{Ca}$  particles are also visible within dimples present across the fracture surface of both specimens. By comparing Figures 12(a) and 12(b), it can be observed that the M75 specimen exhibited a more ductile fracture compared to the M15 specimen. This is consistent with the higher total elongation observed in the M75 specimen, which can be attributed to the partial spheroidization of  $\text{Cu}_5\text{Ca}$  intermetallic particles in the M75 specimen.

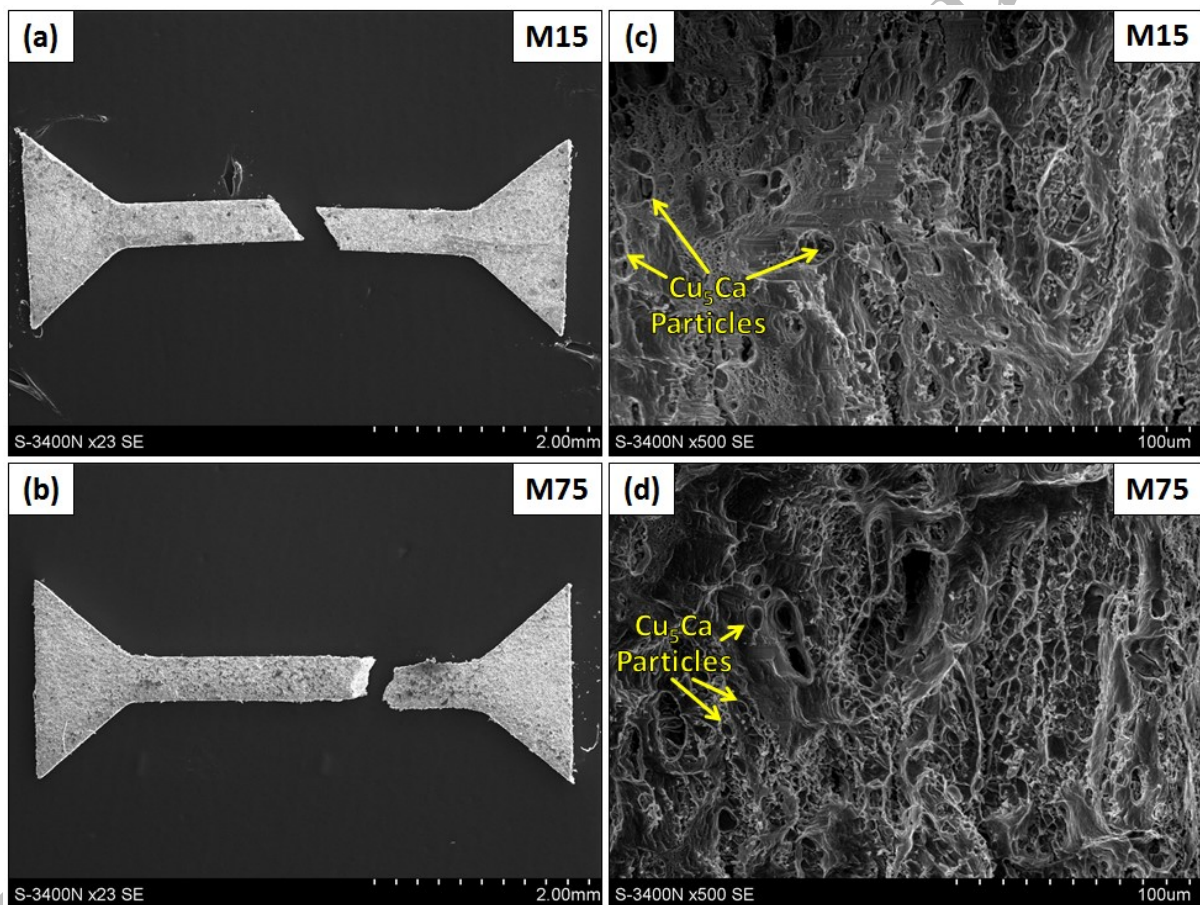


**Figure 12:** The fractured pieces of (a) M15, and (b) M75 specimens; fracture surface of (c) M15, and (d) M75 specimens.

### 3.5. Electrical Conductivity

According to the values recorded as the electrical conductivity of the specimens represented in Figure 13, the A15 specimen possessed a conductivity of  $33.9 \pm 2.6$  MS/m (58.4% IACS), same as the value for the A75 specimen ( $33.9 \pm 2.1$  MS/m). The fact that the conductivities of both the A15 and A75 specimens are 41.6% lower compared to annealed pure copper (58 MS/m [10]) is the result of the Mg-induced solid-solution as well as the presence of  $\text{Cu}_5\text{Ca}$  intermetallic particles in their microstructure. Moreover, the identical electrical conductivity values for the A15 and A75 specimens indicate that conductivity was independent of both annealing duration and cooling rate. The results also show that the application of



MaxStrain processing has led to an approximately 1% reduction in the conductivities of the specimens, as evidenced by the conductivity value of the M15 specimen measured  $33.6 \pm 1.9$  MS/m (57.9% IACS) and the M75 specimen recorded  $33.5 \pm 2.2$  MS/m (57.8% IACS). This can be attributed to the introduction of a higher percentage of HAGBs and crystallographic defects, including point defects and dislocations, within both the M15 and M75 specimens during the MaxStrain processing, which contributed to a more pronounced electron scattering within these specimens and their lower electrical conductivity [55]. It should also be noted that future research could investigate the optimization of deformation parameters, such as temperature and strain rate, to preserve electrical conductivity in MaxStrain processing. This approach could provide valuable insights into enhancing the efficiency and performance of materials processed through this method.

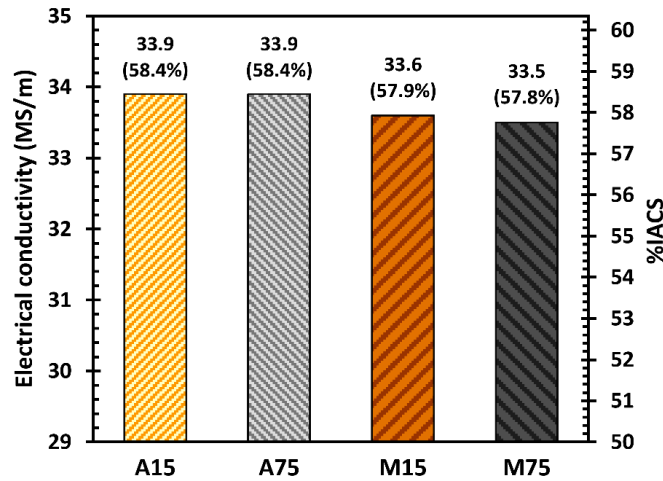


**Figure 13:** Measured values for electrical conductivity of the initial and MaxStrain-deformed specimens.

In conclusion, the findings related to both the microstructural features and the mechanical properties of the developed specimens clearly demonstrate the potential of the MaxStrain process as an effective tool for investigating the impact of various processing parameters, such as deformation magnitude, strain rate, and temperature, on the microstructure, mechanical behavior, and physical properties of metallic materials. However, the widespread implementation of the MaxStrain process still remains limited to research and experimental studies due to several factors, including the time-intensive nature of the process, the lack of continuous production capabilities, and limitations in specimen size. Addressing these limitations through technological advancements and optimized material selection could enhance the practical applicability of the MaxStrain process and make it a more viable option for industrial material processing.

#### 4. Conclusions

The microstructure, mechanical properties, and electrical conductivity of a Cu-0.7Mg-0.1Ca (wt%) alloy were evaluated after undergoing different annealing processes followed by severe plastic deformation using the MaxStrain component of the Gleeble thermo-mechanical testing device. The results of this research lead to the following conclusions:

- (1) Annealing for 75 min at 923 K followed by quenching in agitated water (A75 specimen) resulted in the homogenization of the distribution of magnesium atoms within the single-phase Cu-Mg matrix, partial spheroidization of Cu<sub>5</sub>Ca intermetallic particles, and the introduction of residual thermal stresses in the A75 specimen. Compared to the A15 specimen (which underwent 15 min of annealing at 923 K followed by cooling in the air), these effects of the annealing and subsequent quenching led to a 4% increase in hardness, a 5% increase in yield strength, a 4% increase in tensile strength, and a 6% increase in elongation.
- (2) The simulation results revealed a non-uniform pattern of equivalent strain within the specimens after undergoing 20 passes of MaxStrain deformation. In both specimens, the strain gradient influenced the hardness distribution, with the highest hardness recorded at the center, corresponding to the highest equivalent strain, and decreasing towards the edges.

(3) The residual thermal stresses in the M75 specimen promoted the occurrence of DRX during MaxStrain processing, as demonstrated by a greater proportion of grains exhibiting GOS quantities below 2° in the M75 specimen in comparison to the M15 specimen. Moreover, the M75 specimen exhibited a smaller mean grain size and a greater number of HAGBs. In both M15 and M75 specimens, some cracks were observed in non-deformed Cu<sub>5</sub>Ca particles.

(4) MaxStrain processing significantly enhanced yield strength, with the M15 and M75 specimens showing increases of 229% and 232% compared to their non-deformed counterparts (A15 and A75), respectively. The tensile strengths also improved, with increases of 86% and 91% for M15 and M75, respectively. However, this improvement came at the cost of decreasing ductility, with both M15 and M75 exhibiting reductions in elongation of 48% and 44%, respectively.

(5) The electrical conductivities of non-deformed specimens were found to be independent of annealing duration and cooling rate. Moreover, while MaxStrain processing increased the strength of both specimens, it also led to a decrease in their electrical conductivity by approximately 1%. Nonetheless, all MaxStrain-deformed specimens met the minimum electrical conductivity requirements while also exhibiting the necessary mechanical properties to qualify as HSHC copper alloys.

## Acknowledgements

This study was funded by the Silesian University of Technology under project number 11/030/BK\_24/1177. The authors would like to thank the Faculty of Materials Engineering at the Silesian University of Technology and the Laboratory for Mechanics of Materials and Nanostructures at the Swiss Federal Laboratories for Materials Science and Technology (Empa) for their valuable collaboration and technical support, which were essential for completing this research.

## Declaration of Generative AI and AI-assisted Technologies in the Writing Process

During the preparation of this work, the authors used ChatGPT-3.5 in order to detect and correct any grammatical mistakes. After using this tool, the authors reviewed and edited the content as needed and take full responsibility for the content of the publication.

## Data Availability:

The raw/processed data required to reproduce the above findings cannot be shared at this time as the data also forms part of an ongoing study.

## References

- [1] B. Grzegorzczuk, S. Rusz, P. Snopinski, O. Hilser, A. Skowronek, A. Grajcar, Effect of ECAP process on deformability, microstructure and conductivity of CuCoNi alloy, *Journal of Mining and Metallurgy, Section B: Metallurgy*. 59 (2023) 39–51.
- [2] J.G. Ke, R. Liu, Z.M. Xie, L.C. Zhang, X.P. Wang, Q.F. Fang, C.S. Liu, X.B. Wu, Ultrahigh strength, thermal stability and high thermal conductivity in hierarchical nanostructured Cu-W alloy, *Acta Materialia*. 264 (2024) 119547. <https://doi.org/10.1016/j.actamat.2023.119547>.
- [3] Y. Wu, W. Zhang, Y. Li, F. Yang, H. Liu, J. Zou, J. Jiang, F. Fang, A. Ma, An overview of microstructure regulation treatment of Cu-Fe alloys to improve strength, conductivity, and electromagnetic shielding, *Journal of Alloys and Compounds*. 1002 (2024) 175425. <https://doi.org/10.1016/j.jallcom.2024.175425>.
- [4] M. Maleki, M.J. Sohrabi, H. Farzad, H. Mirzadeh, M.H. Parsa, R. Miresmaeili, S.H. Razavi, Unraveling the effect of trace sulfur content on hot working behavior of Cu-DHP alloy: A study using processing maps, *Materials Chemistry and Physics*. 339 (2025) 130739. <https://doi.org/10.1016/j.matchemphys.2025.130739>.
- [5] Z.Q. Chu, K.X. Wei, W. Wei, I. V Alexandrov, X.L. An, D.D. Wang, X.K. Liu, Simultaneously enhancing mechanical properties and electrical conductivity of Cu-0.5%Cr alloy as 5G connector material, *Journal of Alloys and Compounds*. 948 (2023) 169750. <https://doi.org/10.1016/j.jallcom.2023.169750>.
- [6] S. Tang, M. Zhou, Y. Zhang, D. Xu, Z. Zhang, X. Zheng, D. Li, X. Li, B. Tian, Y. Jia, Y. Liu, A.A. Volinsky, E.S. Marchenko, Improved microstructure, mechanical properties and electrical conductivity of the Cu–Ni–Sn–Ti–Cr alloy due to Ce micro-addition, *Materials Science and Engineering: A*. 871 (2023) 144910. <https://doi.org/10.1016/j.msea.2023.144910>.

- [7] Y. Wang, B. Zhong, J. Ni, J. Song, Y. Huang, S. Yao, Y. Liu, T. Fan, Enhanced electrical conductivity of copper by nitrogen-doped graphene, *Scripta Materialia*. 239 (2024) 115797. <https://doi.org/10.1016/j.scriptamat.2023.115797>.
- [8] A. Kalhor, J. Dykas, K. Rodak, A. Grajcar, Materials and constructional design for electric vehicles: A review, *Advances in Science and Technology Research Journal*. 19 (2025) 178–196. <https://doi.org/10.12913/22998624/195457>.
- [9] Q. Mao, Y. Liu, Y. Zhao, A review on copper alloys with high strength and high electrical conductivity, *Journal of Alloys and Compounds*. 990 (2024) 174456. <https://doi.org/10.1016/j.jallcom.2024.174456>.
- [10] X. Tang, X. Chen, F. Sun, P. Liu, H. Zhou, S. Fu, The current state of CuCrZr and CuCrNb alloys manufactured by additive manufacturing: A review, *Materials & Design*. 224 (2022) 111419. <https://doi.org/10.1016/j.matdes.2022.111419>.
- [11] H. Wu, T. Huang, K. Song, Y. Zhou, S. Li, X. Peng, Y. Hua, Y. Xu, X. Han, X. Luo, Microstructure and properties of single crystal copper prepared by hot type horizontal continuous casting process, *Materials Science and Engineering: A*. 927 (2025) 147924. <https://doi.org/10.1016/j.msea.2025.147924>.
- [12] K. Maki, Y. Ito, H. Matsunaga, H. Mori, Solid-solution copper alloys with high strength and high electrical conductivity, *Scripta Materialia*. 68 (2013) 777–780. <https://doi.org/10.1016/j.scriptamat.2012.12.027>.
- [13] M. Xie, W. Huang, H. Chen, L. Gong, W. Xie, H. Wang, B. Yang, Microstructural evolution and strengthening mechanisms in cold-rolled Cu–Ag alloys, *Journal of Alloys and Compounds*. 851 (2021) 156893. <https://doi.org/10.1016/j.jallcom.2020.156893>.
- [14] Y. Jiang, X. Zhang, P. Cai, P. Li, F. Cao, F. Gao, S. Liang, Precipitation behavior and microstructural evolution during thermo-mechanical processing of precipitation hardened Cu–Hf based alloys, *Acta Materialia*. 245 (2023) 118659. <https://doi.org/10.1016/j.actamat.2022.118659>.
- [15] K. Yang, Y. Wang, M. Guo, H. Wang, Y. Mo, X. Dong, H. Lou, Recent development of advanced precipitation-strengthened Cu alloys with high strength and conductivity: A review, *Progress in Materials Science*. (2023) 101141. <https://doi.org/10.1016/j.pmatsci.2023.101141>.
- [16] C. Wang, H. Fu, H. Zhang, X. He, J. Xie, Simultaneous enhancement of mechanical and electrical properties of Cu–Ni–Si alloys via thermo-mechanical process, *Materials Science and Engineering: A*. 838 (2022) 142815. <https://doi.org/10.1016/j.msea.2022.142815>.
- [17] T. Guo, Y. Gao, X. Tai, J. Wang, R. Feng, D. Qian, Y. Ding, Z. Jia, Micro/nanostructure high strength and high conductivity CuCrZr alloy prepared through equal channel angular pressing and aging treatment, *Materials Today Communications*. 33 (2022) 104381. <https://doi.org/10.1016/j.mtcomm.2022.104381>.
- [18] S.A. Hosseini, H.D. Manesh, High-strength, high-conductivity ultra-fine grains commercial pure copper produced by ARB process, *Materials & Design*. 30 (2009) 2911–2918. <https://doi.org/10.1016/j.matdes.2009.01.012>.
- [19] A. Habibi, M. Ketabchi, M. Eskandarzadeh, Nano-grained pure copper with high-strength and high-conductivity produced by equal channel angular rolling process, *Journal of Materials Processing Technology*. 211 (2011) 1085–1090. <https://doi.org/10.1016/j.jmatprotec.2011.01.009>.
- [20] L. Zeng, X. Lu, S. Li, J. Zhang, A nanolaminated structure design to produce high-strength Cu alloys with enhanced electrical conductivity and thermal stability, *Materials Characterization*. 223 (2025) 114883. <https://doi.org/10.1016/j.matchar.2025.114883>.
- [21] L.W. Kong, X.L. Zhu, Z.B. Xing, Y.Q. Chang, H. Huang, Y. Shu, Z.X. Qi, B. Wen, P. Li, Preparation and mechanisms of Cu–Ag alloy fibers with high strength and high conductivity, *Materials Science and Engineering: A*. 895 (2024) 146219. <https://doi.org/10.1016/j.msea.2024.146219>.
- [22] L. Wang, S. Qu, H. Fu, X. Zhou, Z. Hu, Y. Wen, B. Zhang, B. Gan, X. Song, Y. Lu, Additively manufactured copper alloy with heterogeneous nanoprecipitates-dislocation architecture for superior strength-ductility-conductivity synergy, *Additive Manufacturing*. 84 (2024) 104100. <https://doi.org/10.1016/j.addma.2024.104100>.
- [23] H. Wu, T. Huang, K. Song, Y. Zhou, S. Li, Y. Zhang, Effect of large deformation on microstructure and properties of copper alloy wire, *Journal of Materials Research and Technology*. 29 (2024) 5136–5148. <https://doi.org/10.1016/j.jmrt.2024.02.153>.
- [24] F. Han, Y. Jiang, F. Cao, L. Han, J. Zhu, W. Wang, S. Liang, Enhanced strength, ductility and electrical conductivity of CuCrZr alloys by tailoring a heterogeneous layered microstructure, *Materials Science and Engineering: A*. 863 (2023) 144502. <https://doi.org/10.1016/j.msea.2022.144502>.
- [25] H. Song, J. Mai, Z. Zhang, A. Gu, Y. Mai, Y. Chang, A high strength and high electrical conductivity copper based composite enhanced by graphene and Al<sub>2</sub>O<sub>3</sub> nanoparticles, *Materials Science and Engineering: A*. 899 (2024) 146432. <https://doi.org/10.1016/j.msea.2024.146432>.
- [26] W. Xue, G. Xie, X. Huang, J. Liang, S. Guo, X. Liu, X. Liu, Achieving high strength and high-electrical-conductivity of Cu–Ni–Si alloys via regulating nanoprecipitation behavior through simplified process, *Journal of Materials Science & Technology*. 216 (2025) 121–129. <https://doi.org/10.1016/j.jmst.2024.07.039>.
- [27] H. Yang, Z. Ma, C. Lei, L. Meng, Y. Fang, J. Liu, H. Wang, High strength and high conductivity Cu alloys: A review, *Science China Technological Sciences*. 63 (2020) 2505–2517. <https://doi.org/10.1007/s11431-020-1633-8>.

- [28] Y. Li, Z. Xiao, Z. Li, Z. Zhou, Z. Yang, Q. Lei, Microstructure and properties of a novel Cu-Mg-Ca alloy with high strength and high electrical conductivity, *Journal of Alloys and Compounds*. 723 (2017) 1162–1170. <https://doi.org/10.1016/j.jallcom.2017.06.155>.
- [29] Y. Yuan, Z. Li, Z. Xiao, Z. Zhao, Investigations on Voids Formation in Cu–Mg Alloy During Continuous Extrusion, *JOM*. 69 (2017) 1696–1700. <https://doi.org/10.1007/s11837-017-2469-5>.
- [30] M. Ma, Z. Li, W. Qiu, Z. Xiao, Z. Zhao, Y. Jiang, Microstructure and properties of Cu–Mg–Ca alloy processed by equal channel angular pressing, *Journal of Alloys and Compounds*. 788 (2019) 50–60. <https://doi.org/10.1016/j.jallcom.2019.01.335>.
- [31] M. Ma, Z. Li, W. Qiu, Z. Xiao, Z. Zhao, Y. Jiang, Z. Xia, H. Huang, Development of homogeneity in a Cu-Mg-Ca alloy processed by equal channel angular pressing, *Journal of Alloys and Compounds*. 820 (2020) 153112. <https://doi.org/10.1016/j.jallcom.2019.153112>.
- [32] Y. Ru, Z. Gao, L. Zhang, Z. Tang, T. Zuo, J. Xue, L. Xiao, X. Li, Microstructure and Properties of High Strength and High Conductivity Cu-0.4Mg Alloy Processed by Upward Continuous Casting and Multi-pass Drawing, *Journal of Materials Engineering and Performance*. (2023). <https://doi.org/10.1007/s11665-023-08283-9>.
- [33] B. Wang, Y. Zhang, B. Tian, J. An, A.A. Volinsky, H. Sun, Y. Liu, K. Song, Effects of Ce addition on the Cu-Mg-Fe alloy hot deformation behavior, *Vacuum*. 155 (2018) 594–603. <https://doi.org/10.1016/j.vacuum.2018.06.006>.
- [34] B. Wang, Y. Zhang, B. Tian, V. Yakubov, J. An, A.A. Volinsky, Y. Liu, K. Song, L. Li, M. Fu, Effects of Ce and Y addition on microstructure evolution and precipitation of Cu-Mg alloy hot deformation, *Journal of Alloys and Compounds*. 781 (2019) 118–130. <https://doi.org/10.1016/j.jallcom.2018.12.022>.
- [35] A. Kalhor, K. Rodak, M. Tkocz, H. Myalska-Głowacka, I. Schindler, Ł. Poloczek, K. Radwański, H. Mirzadeh, M. Grzenik, K. Kubiczek, M. Kampik, Tailoring the microstructure, mechanical properties, and electrical conductivity of Cu–0.7Mg alloy via Ca addition, heat treatment, and severe plastic deformation, *Archives of Civil and Mechanical Engineering*. 24 (2024) 71. <https://doi.org/10.1007/s43452-024-00890-0>.
- [36] A. Ma, C. Zhu, J. Chen, J. Jiang, D. Song, S. Ni, Q. He, Grain refinement and high-performance of equal-channel angular pressed Cu-Mg alloy for electrical contact wire, *Metals*. 4 (2014) 586–596. <https://doi.org/10.3390/met4040586>.
- [37] P. Rodríguez-Calvillo, N. Ferrer, J.M. Cabrera, Analysis of microstructure and strengthening in CuMg alloys deformed by equal channel angular pressing, *Journal of Alloys and Compounds*. 626 (2015) 340–348. <https://doi.org/10.1016/j.jallcom.2014.12.043>.
- [38] M. Ma, X. Zhang, Z. Li, Z. Xiao, H. Jiang, Z. Xia, H. Huang, Effect of Equal Channel Angular Pressing on Microstructure and Mechanical Properties of a Cu-Mg Alloy, *Crystals*. 10 (2020). <https://doi.org/10.3390/cryst10060426>.
- [39] A. Bodyakova, M. Tkachev, A. Pilipenko, A. Belyakov, R. Kaibyshev, Effect of deformation methods on microstructure, texture, and properties of a Cu–Mg alloy, *Materials Science and Engineering: A*. 876 (2023) 145126. <https://doi.org/10.1016/j.msea.2023.145126>.
- [40] S. Pan, J. Yu, J. Han, Y. Zhang, Q. Peng, M. Yang, Y. Chen, X. Huang, R. Shi, C. Wang, X. Liu, Customized development of promising Cu-Cr-Ni-Co-Si alloys enabled by integrated machine learning and characterization, *Acta Materialia*. 243 (2023) 118484. <https://doi.org/10.1016/j.actamat.2022.118484>.
- [41] M. Mezbahul-Islam, A. Mostafa, M. Medraj, Essential magnesium alloys binary phase diagrams and their thermochemical data, *Journal of Materials*. 14 (2014). <https://doi.org/10.1155/2014/704283>.
- [42] D. Risold, B. Hallstedt, L.J. Gauckler, H.L. Lukas, S.G. Fries, Thermodynamic optimization of the Ca-Cu and Sr-Cu systems, *Calphad*. 20 (1996) 151–160. [https://doi.org/10.1016/S0364-5916\(96\)00022-3](https://doi.org/10.1016/S0364-5916(96)00022-3).
- [43] I. Schindler, P. Kawulok, K. Konečná, M. Sauer, H. Navrátil, P. Opěla, R. Kawulok, S. Rusz, Simulation of Hot Continuous Rolling of a Plain Carbon Steel Using the MAXStrain II® Multi-Axis Deformation System, *Archives of Metallurgy and Materials*. 68 (2023) 741–747. <https://doi.org/10.24425/amm.2023.142456>.
- [44] V. Komarov, I. Khmelevskaya, G. Korpala, R. Kawalla, S. Prokoshkin, Metal Forming Aspects of Cyclic Severe Plastic Deformation of Ti-Ni Shape Memory Alloys Using MaxStrain Device, in: *Key Engineering Materials*, Trans Tech Publ, 2017: pp. 214–218.
- [45] H. Petryk, S. Stupkiewicz, R. Kuziak, Grain refinement and strain hardening in IF steel during multi-axis compression: Experiment and modelling, *Journal of Materials Processing Technology*. 204 (2008) 255–263. <https://doi.org/10.1016/j.jmatprotec.2007.11.068>.
- [46] H. Lin, C. Lu, C. Liu, C. Chen, D. Chen, J.-C. Kuo, K.N. Tu, Microstructure control of unidirectional growth of  $\eta$ -Cu<sub>6</sub>Sn<sub>5</sub> in microbumps on  $\langle 111 \rangle$  oriented and nanotwinned Cu, *Acta Materialia*. 61 (2013) 4910–4919. <https://doi.org/10.1016/j.actamat.2013.04.056>.
- [47] A.R. Alian, Y. Ju, S.A. Meguid, Comprehensive atomistic modeling of copper nanowires-based surface connectors, *Materials & Design*. 175 (2019) 107812. <https://doi.org/10.1016/j.matdes.2019.107812>.
- [48] G. Bruzzone, The binary systems calcium-copper, strontium-copper and barium-copper, *Journal of the Less Common Metals*. 25 (1971) 361–366. [https://doi.org/10.1016/0022-5088\(71\)90178-0](https://doi.org/10.1016/0022-5088(71)90178-0).



- [49] L. Lapeire, J. Sidor, P. Verleysen, K. Verbeken, I. De Graeve, H. Terryn, L.A.I. Kestens, Texture comparison between room temperature rolled and cryogenically rolled pure copper, *Acta Materialia*. 95 (2015) 224–235. <https://doi.org/10.1016/j.actamat.2015.05.035>.
- [50] A. Gupta, T.-H. Yoo, L. Kaushik, J.W. Lee, Y.-K. Kim, S.-H. Choi, Unveiling the room-temperature softening phenomenon and texture evolution in room-temperature- and cryogenic-rolled ETP copper, *International Journal of Plasticity*. 156 (2022) 103340. <https://doi.org/10.1016/j.ijplas.2022.103340>.
- [51] G. Xin, M. Zhou, K. Jing, H. Hu, Z. Li, Y. Zhang, C. Tian, Y. Sun, B. Tian, X. Li, A.A. Volinsky, J. Zou, Hot deformation behavior and microstructure evolution of the Cu-1.5Ti-(0.5Fe) alloys, *Journal of Materials Research and Technology*. 30 (2024) 4961–4972. <https://doi.org/10.1016/j.jmrt.2024.04.208>.
- [52] Y. ZHANG, P. LIU, B. TIAN, Y. LIU, R. LI, Q. XU, Hot deformation behavior and processing map of Cu–Ni–Si–P alloy, *Transactions of Nonferrous Metals Society of China*. 23 (2013) 2341–2347. [https://doi.org/10.1016/S1003-6326\(13\)62739-9](https://doi.org/10.1016/S1003-6326(13)62739-9).
- [53] Y. Liu, H. Huang, J. Xie, Effect of compression direction on the dynamic recrystallization behavior of continuous columnar-grained CuNi10Fe1Mn alloy, *International Journal of Minerals, Metallurgy, and Materials*. 22 (2015) 851–859. <https://doi.org/10.1007/s12613-015-1142-7>.
- [54] G. Yang, Z. Li, Y. Yuan, Q. Lei, Microstructure, mechanical properties and electrical conductivity of Cu–0.3Mg–0.05Ce alloy processed by equal channel angular pressing and subsequent annealing, *Journal of Alloys and Compounds*. 640 (2015) 347–354. <https://doi.org/10.1016/j.jallcom.2015.03.218>.
- [55] K. Zhou, Y. Zhao, H. Dong, Q. Mao, S. Jin, M. Feng, R. Zhang, S. Li, J. Liu, Fractal structure and nano-precipitates break comprehensive performance limits of CuCrZr alloys, *Nano Today*. 56 (2024) 102234. <https://doi.org/10.1016/j.nantod.2024.102234>.

--

## Figure Captions:

Figure 1: Simplified graphical representation of the MaxStrain component of the Gleeble thermo-mechanical testing device shown in (a) 2D (side view) and (b) 3D views.

Figure 2: Schematic of strike pattern for MaxStrain deformation in this study.

Figure 3: Geometrical parameters of tensile test mini specimens (units are in mm).

Figure 4: Simplified schematic representation of the four-wire Kelvin resistance testing device.

Figure 5: (a) SEM-BSE image, and element mapping analysis results for (b) copper, (c) magnesium, and (d) calcium elements in A15 specimen; (e) SEM-BSE image, and element mapping analysis results for (f) copper, (g) magnesium, and (h) calcium elements in A75 specimen; EDS results for (i) area 1, and (j) area 2 marked in (e).

Figure 6: Simulation results showing the pattern of equivalent strain in (a) central transverse, (b) central longitudinal (X-Z), and (c) central longitudinal (X-Y) planes.

Figure 7: (a) IPF map, and (b) GOS map of the M15 specimen; (c) IPF map, and (d) GOS map of the M75 specimen.

Figure 8: Schematic illustrations of the crystal structures of (a) copper [41], and (b) Cu<sub>5</sub>Ca [42] unit cells.

Figure 9: Distribution pattern of misorientation angles (a) M15, and (b) M75 specimens.

Figure 10: SEM-BSE images of Cu<sub>5</sub>Ca intermetallic particles in (a) M15, and (b) M75 specimens.

Figure 11: Hardness test results for (a) M15, and (b) M75 specimens; tensile test results for (c) initial, and (d) MaxStrain-deformed specimens.

Figure 12: The fractured pieces of (a) M15, and (b) M75 specimens; fracture surface of (c) M15, and (d) M75 specimens.

Figure 13: Measured values for electrical conductivity of the initial and MaxStrain-deformed specimens.

--

## Table Captions:

Table 1: Elemental composition of the as-cast material.

Table 2: The summary of processing steps and abbreviated names of the specimens.

JMMB\_accepted\_manuscript